Self-Adaptive Diagnostic of Radial Fast-Ion Loss Measurements on the ASDEX Upgrade Tokamak

J. Gonzalez Martin,[1,2,a)] M. Garcia-Munoz,[2,3] B. Sieglin,[4] A. Herrmann,[4] T. Lunt,[4] J. Ayllon-Guerola,[1,2] J. Galdon-Quiroga,[2] J. Hidalgo-Salaverri,[2] A. Kovacsik,[5] J.F. Rivero-Rodriguez,[1,2] L. Sanchis,[6] D. Silvagni,[4] S. Zoletnik,[7] J. Dominguez,[1] ASDEX Upgrade team,[b)] and MST1 team[c)]

[1)] *Department of Mechanical Engineering and Manufacturing, University of Seville Spain*
[2)] *Centro Nacional de Aceleradores (CNA), Universidad de Sevilla, CSIC, Junta de Andalucía*
[3)] *Department of Atomic, Molecular and Nuclear Physics, University of Seville, Spain*
[4)] *Max-Planck-Institut für Plasmaphysik, Garching, Germany*
[5)] *Budapest University of Technology and Economics, Budapest, Hungary*
[6)] *Department of Applied Physics, Aalto University, FI-00076, Aalto, Finland*
[7)] *Wigner RCP, Budapest, Hungary*

(Dated: 14 December 2020)

A poloidal array of scintillator based Fast-Ion Loss Detectors (FILD) has been installed in the ASDEX Upgrade (AUG) tokamak. While all AUG FILD systems are mounted on reciprocating arms driven externally by servo-motors, the reciprocating system of the FILD probe just below the midplane is based on a magnetic coil that is energized in real-time by the AUG discharge control system. This novel reciprocating system allows, for the first time, real-time control of the FILD position including infrared measurements of its probe head temperature to avoid overheating. This considerably expands the diagnostic operational window, enabling unprecedented radial measurements of fast-ion losses.
Fast collimator-slit sweeping (up to 0.2 mm/ms) is used to obtain radially resolved velocity-space measurements along 8 cm within the scrape-off-layer. This provides a direct evaluation of the neutral beam deposition profiles via first-orbit losses. Moreover, the light ion beam probe (LIBP) technique is used to infer radial profiles of fast-ion orbit deflection. This radial-LIBP technique is applied to trapped orbits (exploring both the plasma core and the FILD stroke near the wall), enabling radial localization of internal plasma fluctuations (neoclassical tearing modes). This is quantitatively compared against electron cyclotron emission (ECE) measurements showing excellent agreement. For the first time, radial profiles of fast-ion losses in MHD quiescent plasmas as well as in the presence of magnetic islands and ELMs are presented.

Draft to be submitted to Review of Scientific Instruments related to an invited talk (T5H17) on the 23rd High Temperature Plasma Diagnostics (HTPD2020) conference.

I. INTRODUCTION

To ignite a magnetically-confined plasma, fast-ions created by auxiliary heating systems (neutral beam injectors (NBI) and ion-cyclotron resonance heating (ICRH)) must be confined for a sufficient time so that they thermalize thus transferring their energy to the bulk plasma via Coulomb collisions. Moreover, a burning plasma can only be self-sustained if the resulting large population of fusion-born α particles is retained within the plasma, so that it can be used as the primary heating source[1]. On the contrary, if these fast/energetic particles escape the plasma and hit the wall, they might cause serious damage, jeopardizing the integrity of the whole device, especially if these losses are strongly localised.

In this context, aiming at characterizing the mechanisms responsible for classical and non-classical fast-ion transport and losses, the scintillator-based fast-ion loss detector (FILD)[2] provides accurate velocity-space measurements of escaping ions at MHz temporal resolution. In contrast to its many applications, one of the main limitations of this diagnostic consist on the fact that the interrogated phase-space volume is localised as a point in real-space, being impossible to withdraw any conclusion about the spatial dependence of the velocity-space of escaping ions.

On the contrary, the magnetically-driven FILD[3] recently installed in the ASDEX Upgrade tokamak (AUG) is able to adapt its insertion in real-time, enabling access to unexplored physics such as radially-resolved velocity-space measurements and radially resolving the internal perturbations by means of the light-ion beam probe (LIBP) technique.

This manuscript is organized as follows: Section II introduces the FILD working principle along with the FILD poloidal array installed in AUG and its phase-space coverage. In Section III, the magnetically-driven manipulator used to insert FILD in real-time is assessed. Section IV describes the first radially-resolved velocity-space measurements and section V discusses the radial dependence of MHD-induced fast-ion losses. Future applications of this diagnostic are proposed in section VI together with the conclusions of this work.

II. FILD ARRAY IN ASDEX UPGRADE

FILDs work as magnetic spectrometers using incoming ions, which on their gyro-orbits enter the probe head though a

[a)] Electronic mail: jgonzalez62@us.es
[b)] see the author list of H. Meyer et al. 2019 Nucl. Fusion **59** 112014
[c)] see the author list of B. Labit et al. 2019 Nucl. Fusion **59** 0860020

collimator pinhole and impinge onto a scintillator plate. The striking point on the scintillator plate depends on the particle pitch angle and gyroradius (i.e. energy if the ion charge-mass ratio is known). Therefore, FILD provides time-resolved energy and pitch angle measurement of the escaping ions. The very short decay time (bellow 1μs) and high quantum efficiency of the scintillating material, allow us to obtain MHz temporal resolution if the appropriate light acquisition systems are employed. The high temporal resolution can be used to identify intra-ELM mechanisms responsible for the losses.

There are 5 FILDs installed on AUG (figure 1). FILD1, FILD2, FILD3 and (more recently installed) FILD5[4] have their own permanent manipulators[5] to modify their insertion in a shot-to-shot basis. On the other hand, the magnetically-driven manipulator employed on FILD4 enables to adapt its insertion (up to a maximum of 8 cm) during the plasma discharge.

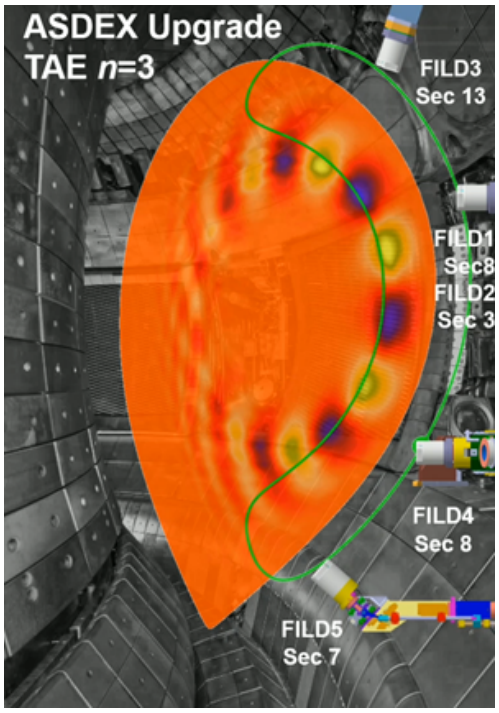

FIG. 1. Poloidal view of the AUG vessel and CAD of the installed FILD systems. A poloidal projection of a trapped particle is included interacting with a toroidicity-induced Alfvén eigenmode on its inner banana leg and captured by the FILDs on its outer leg.

Each FILD covers a bi-dimensional phase-space surface at the edge of the fast-ion distribution. The simultaneous measurements of different phase-space surfaces provided by the FILD array improve the phase-space coverage and helps diagnosing the spatial dependence of the losses on the wall (e.g. ripple, externally applied magnetic perturbations and MHD instabilities). Moreover, the radial scan produced by FILD4 enables to measure a 3D volume in phase-space.

III. MAGNETICALLY-DRIVEN FILD

Before producing radial measurements, the dynamics of the new FILD, the heat loads on the probe head and its light acquisition systems need to be assessed. A more detailed description of the system can be found in references[3,6].

A. Dynamical assessment

The probe head of this in-situ system is constantly being pulled back by a retaining spring. An in-vessel coil is externally energized, creating a magnetic moment along its longitudinal axis that tries to align with the existing toroidal magnetic field of AUG, producing the torque needed to overcome the retaining spring force. The voltage applied to the coil is regulated by a programmable power supply (CAENels FASTPS058400)[7] directly controlled by the discharge control system (DCS) in real time using a TELNET communication protocol. This power supply has the capability of delivering a maximum voltage and current of 80V and 5A respectively, which are regulated within 1 ms. The resulting torque applied on the coil is

$$\tau_{coil} = \frac{NAB\cos(\theta)}{R}\left(V - NAB\cos(\theta)\dot{\theta} - L_{self}\dot{I}\right), \quad (1)$$

being N the number of coil windings, A the coil transversal area, B the toroidal magnetic field at the coil location, R the coil resistance, θ the coil rotation, L_{self} the self inductance, I the electrical current circulating through the coil and V the voltage applied by the power supply. The second term of equation 1 corresponds to the back-electromotive force, damping the system and restricting its velocity but also providing stability. In the last term, the coil self inductance ($L_{self} = \mu_0 N^2 A/h$) is minimized by maximizing the coil height (h) within the design constraints.

The equations governing magnetically-driven manipulators can be found in references[8–10]. Those equations are particularized to the design of this new FILD and linearized around the equilibrium point of $\theta = 0°$. That linear model is integrated in time using a fourth order Runge-Kutta algorithm that converges in time with 1ms time steps. The actual value of the toroidal magnetic field at the coil location is included in the model for each analyzed discharge. As shown on figure 2, those simple simulations are already in good agreement with the measured FILD trajectory. This linear model is used to validate insertion measurements (inferred from the induced back electromotive force coil current[8–10]) and to optimize the scanning cycles used to obtain FILD radial measurements.

B. Thermal assessment

The thermal behaviour of the FILD probe head is simulated for different purposes[11]. The simulated heat load can be subtracted to IR measurements of the probe head to estimate the absolute fast-ion flux on the head[12]. On the other hand, these simulations provide an estimation of the characteristic time of

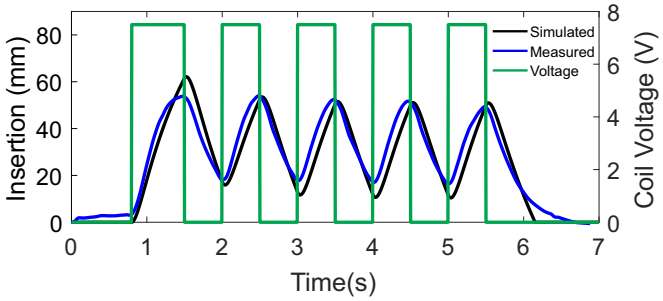

FIG. 2. Predicted and measured FILD trajectories showing insertion/retraction cycles during plasma pulse #36498 with a toroidal magnetic field on axis of B_t=-2.5T and at the FILD coil location of B=-1.9T.

the heating process, helping to set upper boundary limits on the FILD real-time control.

The applied parallel heat load is extrapolated from divertor target measurements (figure 3) using two different exponential decays[13] to account for the near and far scrape-off layer. The applied heat load on each FILD depends on its poloidal location and the incident angle of the magnetic field and probe head surface. Field line 3D tracing is used to calculate the wet (receiving heat flux) surfaces and field line length, which is compared against the collection length[14]. The obtained heat fluxes are applied in a Finite Elements Analysis using ANSYS[15]. The obtained spatial temperature distributions agree well with IR measurements for different FILDs. The predicted temperatures are below the measurements because fast-ion heat flux is not included in the model. Figure 4 shows the simulated evolution of the maximum temperature of the FILD probe head for different duty cycles. One can observe that the heating process is much slower than the typical times ($\sim$ 100ms) required to retract FILD a couple of centimeters to reduce the incident heat flux. One should also note that a duty cycle of 50% (similar case when scanning the FILD insertion) significantly reduces the maximum temperature of the probe head.

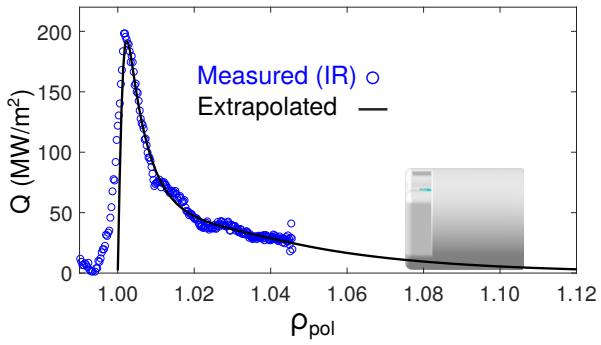

FIG. 3. Measured IR heat flux on the divertor and its extrapolation towards the FILD probe head.

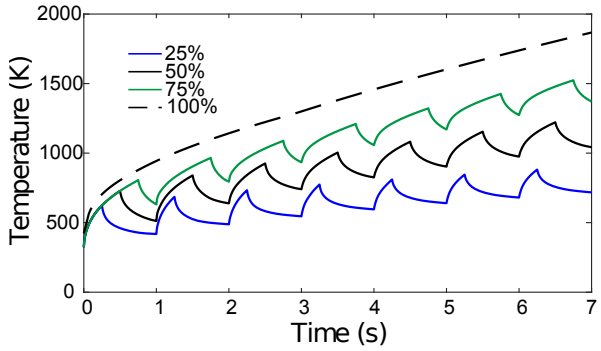

FIG. 4. Predicted evolution of the maximum temperature on the FILD head for different duty cycles.

C. Light acquisition systems

The light pattern emitted by the scintillator plate is simultaneously recorded by two different light acquisition systems. A Charge Couple Device (CCD) camera[16] provides high velocity-space resolution (480x640 pixels) measurements every 20 milliseconds. On the other hand, the high temporal resolution measurements are provided by an Avalanche Photo Diode (APD) camera[17] of 32 pixels recording at a sampling rate up to 2MHz. Both cameras are installed outside the reactor vessel and the light emitted by the scintillator is transported to an anti-reflection coated vacuum window by a 3.5m quartz-made image guide. The thickness of the fibres composing the image guide limits the velocity-space resolution inducing the artifacts observed on figures 6 and 7. This limitation on the velocity-space resolution of the CCD camera does not affect the radial dependence of the measurements.

IV. RADIALLY-RESOLVED VELOCITY-SPACE MEASUREMENTS

When FILD is inserted at a fixed location, its able to produce time-resolved velocity-space measurements at the edge of the fast-ion distribution function. For instance, the new FILD was able to identify passing (trapped) orbits produced by a sequence of applied tangential (radial) beams[3].

While FILD can be moved in a shot to shot basis to infer fast-ion profiles[18], the new diagnostic technique reported on this paper consists on performing consecutive scans on the FILD insertion. If the plasma parameters are constant thought the scanning cycles, the time-resolved fast-ion measurements can be translated into radially-resolved velocity-space measurements.

A. 3D measurements of fast-ion losses

The FILD insertion/retraction cycles are applied to discharges with plasma current $I_p = 0.8$MA and magnetic field $B_t = -1.8$T, producing critical damping on the FILD manipulator, and thus, enabling fast movement of the FILD head

needed for performing insertion/retraction cycles.

Figure 5 shows the time traces of a discharge in which 2.5MW beam sources #3 (60 keV) and #8 (93 keV) are consecutively applied combined with eventual 2.9MW of ICRH power at 30 MHz. Despite the temporal changes in the applied heating systems, the electron density remains practically constant at the core ($n_e = 5.4 \cdot 10^{-19}\mathrm{m}^{-3}$) and edge ($n_e = 3.2 \cdot 10^{-19}\mathrm{m}^{-3}$). The field-line helicity at the edge $q_{95} = 3.8$ is also unperturbed during the whole shot, while electron temperature T_e is sightly modified by the applied heating scheme, remaining relatively constant through each phase.

The inferred evolution of the FILD insertion is depicted on figure 5 (e). One can observe that FILD is fully inserted once the first NBI beam has been applied. Then, after FILD reaches a steady inserted position, the voltage on the magnetic coil is sequentially reversed, forcing the system to oscillate 25mm each 400ms, modulating the measured FILD signal produced by the APD camera. This translates into 25mm radial profiles of fast-ion losses each 200ms. The critical damping on the FILD manipulator produced by the magnetic field on this scenario was crucial to obtain that large number of cycles/second. This ratio could be further increased by optimizing the voltage curve applied on the coil, however, the CCD sampling rate is limited to 20ms, limiting the radial resolution of the velocity-space measurements in case FILD moves faster.

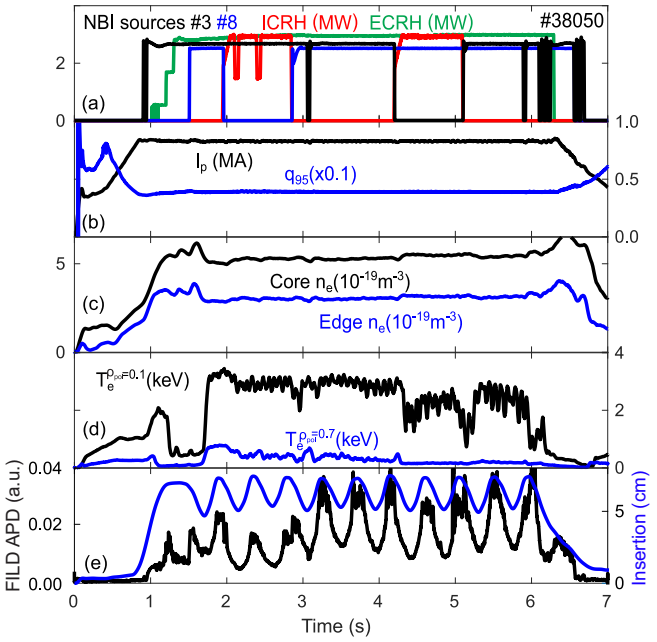

FIG. 5. Time traces of the plasma discharge #38050 showing (a) evolution of applied NBI and ICRH, (b) evolution of plasma current I_p and edge field-line helicity q_{95}, (c) core and edge electron densities n_e, (d) electron temperatures T_e at the core and at $\rho_{pol} = 0.7$, (e) the insertion of the FILD detector and the fast-ion loss level measured by the channel #19 of the FILD APD camera.

For each insertion cycle, one can combine the time-resolved velocity-space measurement with the inferred time-resolved FILD insertion

$$FILD = FILD(Energy, Pitch, Time), \tag{2a}$$

$$R_{FILD} = R_{FILD}(Time), \tag{2b}$$

to produce 3D measurements of the escaping fast-ion population,

$$FILD = FILD(Energy, Pitch, R_{FILD}). \tag{3}$$

Figure 6 illustrates the resulting 3D fast-ion distribution as a 3D contour plot, showing fast-ion losses produced by both NBI and ICRH. To reconstruct the energy of these measurements, deuterium ions are assumed for both NBI and ICRH signals.

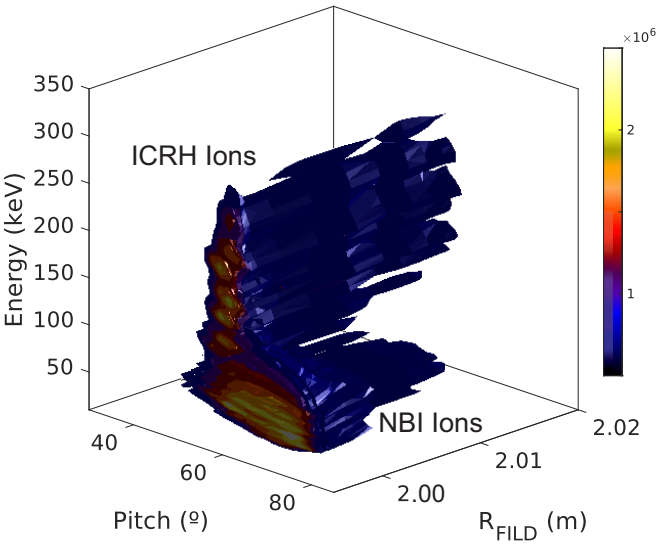

FIG. 6. 3D contour plot of the measured fast-ion distribution on shot #38050 between 4.86 and 5.1 seconds as a function of particle energy (keV), pitch angle (º) and radial location of the FILD collimator slit (m).

B. Radial measurements of NBI and ICRH ions

Figure 7 shows the measured velocity-space pattern at the innermost insertion. The pattern of figure 6 is observed more clearly. This 2D image, normally employed for FILD at fixed location, helps defining regions of interest (ROI) corresponding to both NBI and ICRH ions (green dashed rectangles).

The ROI values are radially plotted over consecutive reciprocating cycles (in which the heating scheme is not modified) in figure 8. The uncertainty of the ROI signal induced by the CCD camera readout noise is smaller than 1%, being negligible when compared to the uncertainty in R_{FILD} (1 mm), induced by the coil resistivity (0.01 Ω) readout. For the sake of clarity, figure 8 includes the error bar associated with a single measurement point. Both NBI and ICRH profiles are obtained from the same CCD frames, hence, any systematic error on

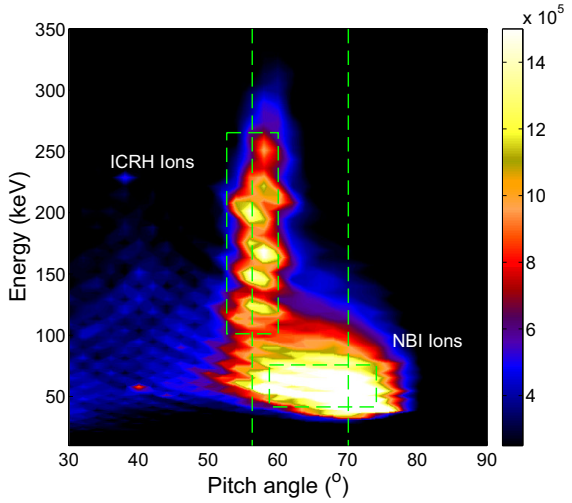

FIG. 7. Measured velocity-space pattern at the innermost insertion for #38050 and 5.1s. Deuterium is assumed for reconstructing the measured energy. The artifacts produced by the image guide can be identified as localized spots on the ICRH region. Regions of interest used to produce figure 8 and pitch-angle interrogated on figure 9 are over plotted.

R_{FILD} displaces both profiles jointly. Despite both heating systems are producing similar levels of signal on FILD, the radial gradient of the measured fast-ion distribution is much larger for NBI than for ICRH ions. This can be qualitatively explained by the fact that NBI ions are deposited at the plasma edge while ICRH ions are generated at the absorption layer at the core.

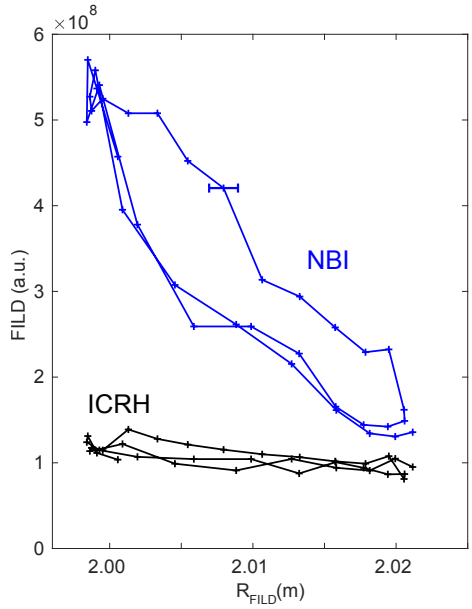

FIG. 8. Radially-resolved ROI values defined for NBI (E⊂ [45,95]keV , Pitch⊂ [58,74]°) and ICRH (E⊂ [100,270]keV , Pitch⊂ [52,60]°) ions over consecutive reciprocating cycles. The NBI ions are observed to have a larger radial gradient than the ICRH population.

Besides the radial evolution of the integrated NBI and ICRH distribution, one can also use the 3D measurements to investigate the radial dependence of the fast-ion energy at each measured pitch angle. On figure 9, the radial profiles at a given pitch angle (°) are plotted for NBI and ICRH ions. For the sake of clarity, these interrogated pitch angles are identified as vertical dashed green lines on figure 7. One can again

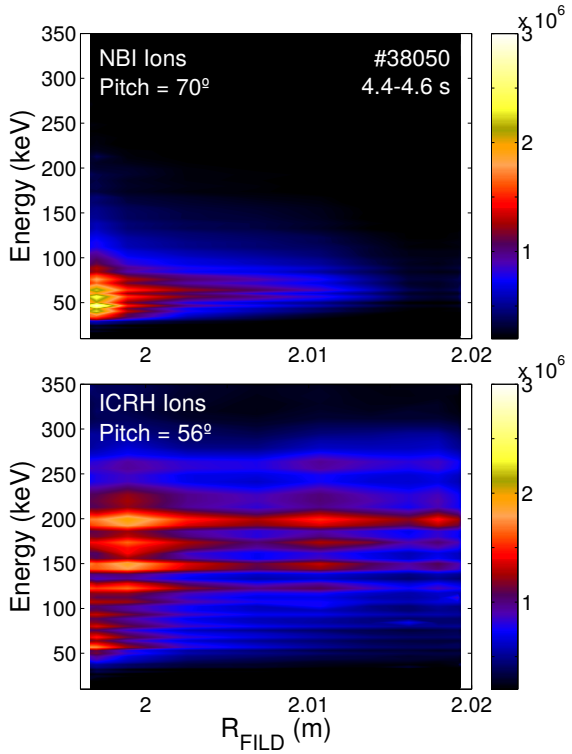

FIG. 9. Radially and energy resolved fast-ion loss measurements for the pitch angles corresponding to NBI ions (70°) and ICRH ions (56°). One can observe that ICRH ions with larger energy have smaller radial gradient than those with low energy.

identify the different radial gradients for ICRH and NBI ions. Furthermore, this measurements help to notice that the radial profile of ICRH ions is different for each energy, having a larger gradient with smaller energy. This novel observations can help validate models that reproduce the fast-ion accelerated ICRH distribution.

C. Radial profiles from different NBI sources

Figure 10(a) depicts the measured velocity-space pattern at the FILD innermost insertion of a phase where NBI sources #6 and #8 (93 keV) are simultaneously applied. Source #6 is tangential while source #8 injects ions more radially. The measured pitch-angle profile at the injected energy is plotted on figure 10(b) together with the predicted losses using the ASCOT[19] code. ASCOT reproduces the measured pitch angle profile and enables to identify the birth location of the ions heating the FILD probe. All the simulated ions injected by NBI source #8 that reach FILD are coming from the high-field

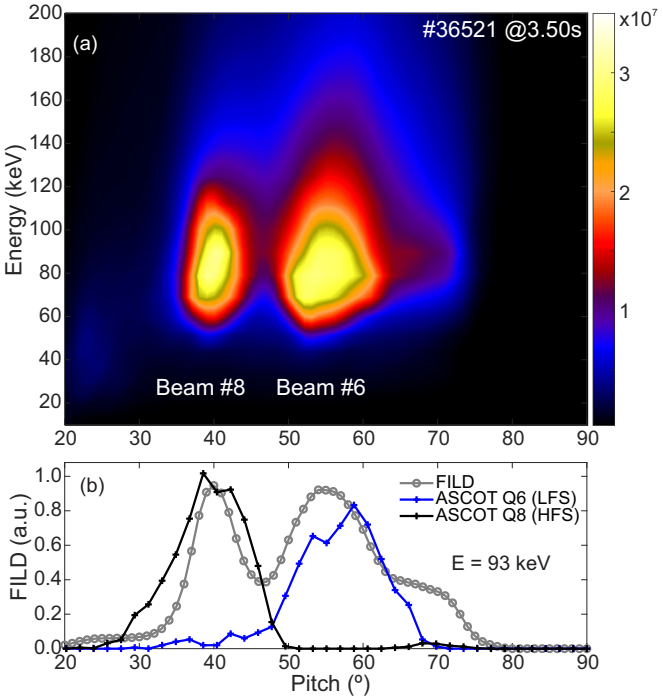

FIG. 10. (a) Measured velocity-space pattern produced by NBI sources #6 and #8. (b) Comparison of measured pitch angle profile at the injection energy (93keV) of measured FILD signal and ASCOT predictions.

side (HFS) of the plasma, while simulated ions injected by source #6 and hitting FILD are ionized both at low-field side (LFS) and HFS. ASCOT simulations help us to conclude that the measured spot corresponds to the particles ionized at the LFS, whereas the particles ionized at the HFS are not captured by FILD in the experiment. This can be explained by the fact that these ions hit FILD with small pitch angle and cannot reach the scintillator plate.

Figure 11 shows the radial profile for the ROIs defined on the measured velocity-space pattern (figure 10) for each beam. One can observe that particles ionized at the LFS are captured ≈1cm earlier by FILD. This can be partially explained by the fact that FILD moves across the passing/lost boundary for particles ionized at the HFS. Another explanation is that particles injected by beam #6 are exploring the plasma core and interacting with internal instabilities that cause orbit deflection, as explained in more detail in section V. The radial profile measured for beam source #8, which is not perturbed by internal fluctuations, has been reproduced by the ASCOT code, showing excellent agreement.

V. RADIALLY-RESOLVED PERTURBATIONS

Besides radially resolving the quiescent velocity-space distribution of fast-ions at the edge, the high temporal resolution of the FILD systems enables to radially resolve fast-ion losses induced by core and edge perturbations.

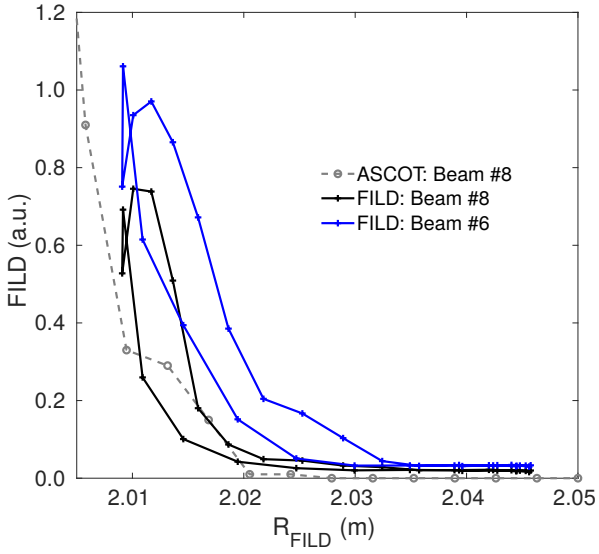

FIG. 11. Measured radial profiles for beam #8 (ionized at the HFS) and #6 (ionized at the LFS). ASCOT simulations reproduce the measured beam deposition profile of source #8.

A. Radial profile of ELM-induced fast-ion losses

Measurements of fast-ion losses induced by Edge Localized Modes (ELMs) have been reported by Garcia-Munoz[20] and Galdon-Quiroga[21] among many other works. The high sampling frequency of the APD camera (up to 2MHz) enables to resolve these losses. Figure 12(a) shows the temporal evolution of the ELM monitor during a FILD insertion/retraction cycle. On figure 12(b) the FILD signal is modulated by its insertion and the spikes induced by the ELMs are clearly visible and isolated using a simple spike detection algorithm.

The radially-resolved ELM-spikes induced on the FILD detector can be collected for all cycles produced during a whole plasma discharge, producing the measurements shown in figure 13. This technique can be employed to study the radial dependence of ELM-induced fast-ion losses under different heating schemes, field-line helicity and, as shown in that example, different applied magnetic fields. The statistics shown in figure 13 are however limited, and thus need to be improved before any physical interpretation of these measurements.

B. Radially-resolved orbit deflection induced by magnetic islands

In scenarios with existing magnetic islands, the position of the FILD probe was scanned, producing the first radially-resolved measurements of coherent fast-ion losses induced by internal perturbations. Figure 14 depicts the time-traces of an example discharge where electron density and plasma current are constant through the entire pulse. 2MW of ECRH power are applied together with a total of 5MW of NBI using sources #6 and #7. At 2.5 seconds, source #7 is replaced by #8. This discharge has a plasma current of $I_p = 0.8$ MA

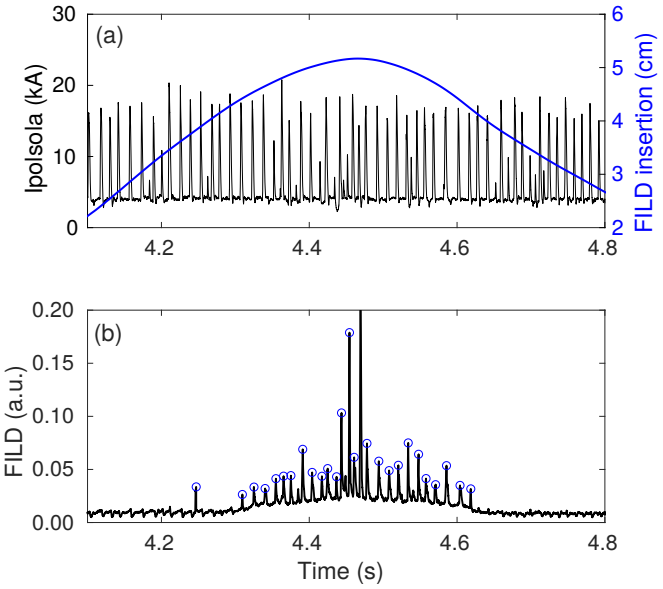

FIG. 12. (a) Temporal evolution of the divertor target current, used as an ELM monitor along with FILD inferred insertion. (b) Measured FILD signal including spikes induced by ELMs.

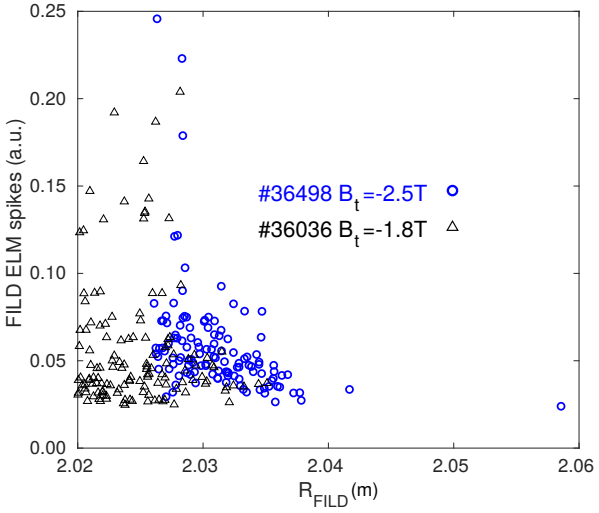

FIG. 13. Measured spikes on the FILD signal induced by ELMs during two different discharges at different magnetic field on axis.

and a magnetic field of $B_t = -2.5$ T, overdamping the FILD movement and thus restricting the achievable number of cycles/second. The FILD trajectory is depicted on figure 14(c) together with the spectrogram of the APD recorded signal, in which the coherent MHD-induced fast-ion losses are visible. The intensity of the measured coherent losses is clearly amplified when the FILD probe is inserted. The Light Ion Beam Probe (LIBP)[22,23] technique is applied to these radial measurements. This technique provides an experimental estimation of the fast-ion orbit radial displacement (ξ) by means of analyzing the modulated FILD signal (ΔF) induced by ions which are lost on their first poloidal transit after a single pass

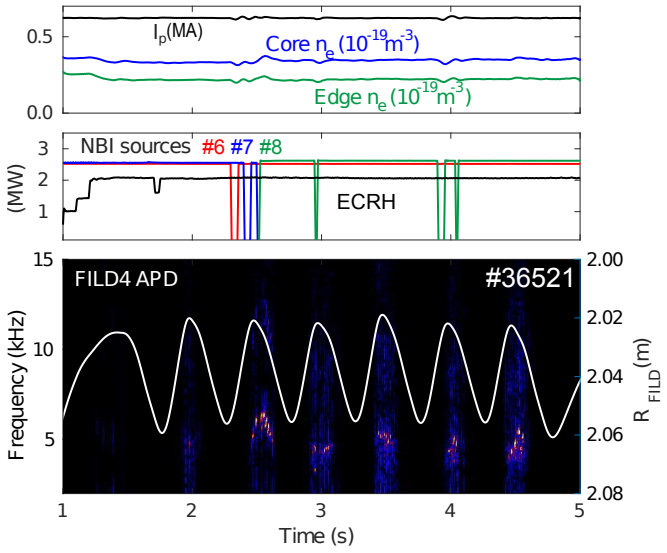

FIG. 14. Overview of discharge #36521 showing (a) temporal evolution of plasma current, core and edge electron densities, (b) applied NBI and ECRH heating and (c) spectrogram of FILD signal showing MHD-induced coherent losses modulated by the FILD insertion.

through the internal perturbation,

$$\xi \approx (\Delta F/\bar{F})L_i. \tag{4}$$

$\bar{F}$ is the unperturbed (mean) fast-ion flux and L_i is the ionization scale length at the orbit birth location, which can be substituted by the density scale length near the edge due to the strong linear dependence of the ionization profile on edge electron density n_e.

The LIBP technique is applied to the time window from 3.3 to 3.7 seconds, when, as seen on figure 14, electron density, applied heating and frequency of the MHD instability are constant. A spectrogram of a magnetic pick-up coil is illustrated in figure 15(a) showing the evolution of the perturbation which has been identified as a Double Tearing Mode (DTM) radially expanding from ρ_{pol} =0.35 to 0.65 and having toroidal and poloidal periodicities of $(n,m) = (1,3)$. Figure 15(b) shows the spectrogram of the coherent FILD signal from the APD camera during the time window of interest. Coherent losses observed at the spectrogram are not only modulated by the FILD insertion, but also by the DTM amplitude. To disentangle this effect, the mode amplitude is tracked as shown on figure 15(a) and smaller time windows on the FILD signal are selected at each local maximum, resulting on samples of FILD measurements at almost constant DTM amplitude and frequency.

The samples of the raw FILD signal, plotted as scattered points on figure 15(c), can be averaged obtaining $\bar{F}$ and Fourier-transformed to obtain the fluctuating component at the DTM frequency (ΔF). The resulting values of $(\bar{F}, \Delta F)$ are analyzed by applying equation 4 to produce time-resolved estimations of the orbit deflection.

Since FILD is performing an insertion/retraction cycle, the radial profile of the orbit deflection is obtained as shown on

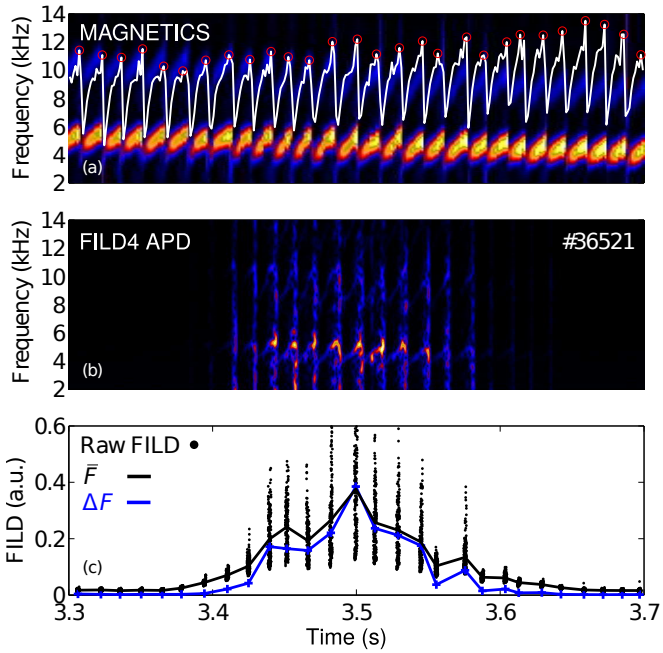

FIG. 15. (a) Magnetic spectrogram of DTM with overlaid tracked amplitude. (b) Spectrogram of the FILD signal showing coherent losses at the same frequency as the DTM. (c) Samples of raw FILD signal together with its mean values and oscillating component at the mode frequency.

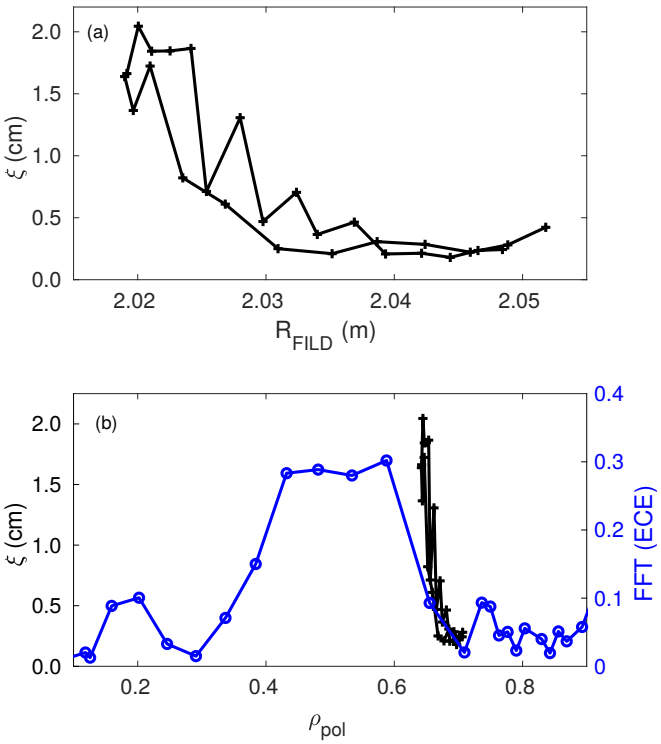

FIG. 16. Radial profile of orbit deflection at the FILD location (a) and at the innermost ρ_{pol} of the measured orbit (b) together with DTM radial structure measured by ECE.

figure 16(a). This radial profile corresponds to the outer banana leg of the measured trapped orbits. Velocity-space measurements reveal that these ions are captured with an energy of $E = 93$keV and pitch angle of 65°. This information is used to track the measured orbits backwards in time to connect the FILD location (R_{FILD}) with the innermost flux surface explored by each orbit, helping to remap the radial profile against the minimum ρ_{pol} of the internal banana leg. This internal profile is compared against the reconstructed mode structure obtained by ECE (figure 16(b)). Despite the limited radial range covered by FILD, the measured dependence of the orbit deflection seems to agree with the reconstructed ECE profile, measuring FILD a larger number of radial points along the covered range when compared to ECE. The FILD internal radial range could be expanded by combining orbits measured by different APD pixels.

VI. OUTLOOK AND SUMMARY

A new FILD system installed in AUG is able to adapt its position during the discharge. Thermal and dynamical simulations are performed to test the feasibility of the scanning cycles, which are used to obtain radially-resolved velocity-space measurements of escaping ions. Since the position of the FILD system is regulated in real-time by the DCS, future control strategies based on any signal or event can be easily implemented. The most natural strategy will be to adapt FILD insertion based on its probe head temperature measured by the safety camera, expanding the operational window to any plasma discharge and optimizing the measurements. But FILD could also react to changes on the position of the last closed flux surface. In addition to this, if the magnetic field of the device is modified, the voltage on the coil could be adapted in real-time, so FILD is fixed at constant insertion.

On the other hand, the first radially-resolved FILD measurements of NBI and ICRH ions are described and compared against simulations. Furthermore, radial profiles of losses induced by edge (ELMs) and internal (DTM) perturbations are described. The LIBP technique is applied to these measurements to resolve the internal radial structure of the DTM. In the future, this radially-resolved LIBP technique can also be applied to a large variety of internal fluctuations, such as Alfvén eigenmodes, magnetic islands and externally applied 3D magnetic perturbations.

ACKNOWLEDGMENTS

The authors would like to show their gratitude to Wolfgang Popken and the entire AUG Vessel Team for their contribution to this work.

This work has been carried out within the framework of the EUROfusion Consortium and has received funding from the Euratom research and training programme 2014-2018 and 2019-2020 under Grant Agreement No. 633053. The views and opinions expressed herein do not necessarily reflect those

of the European Commission.
This research also received funding from the Spanish Ministry of Science under grant No FPU15/06074.
The data that support the findings of this study are available from the corresponding author upon reasonable request.

[1] A. Fasoli, C. Gormenzano, H. L. Berk, B. Breizman, S. Briguglio, D. S. Darrow, N. Gorelenkov, W. W. Heidbrink, A. Jaun, S. V. Konovalov, R. Nazikian, J. M. Noterdaeme, S. Sharapov, K. Shinohara, D. Testa, K. Tobita, Y. Todo, G. Vlad, and F. Zonca, Nuclear Fusion **47**, 264 (2007).
[2] M. García-Muñoz, H.-U. Fahrbach, and H. Zohm, Review of Scientific Instruments **80**, 053503 (2009).
[3] J. Gonzalez-Martin, M. Garcia-Munoz, A. Herrmann, J. Ayllon-Guerola, J. Galdon-Quiroga, A. Kovacsik, P. Leitenstern, T. Lunt, J. Rivero-Rodriguez, B. Sieglin, S. Zoletnik, J. Dominguez, AUG, and M. Teams, Journal of Instrumentation **14**, C11005 (2019).
[4] J. Gonzalez-Martin, J. Ayllon-Guerola, M. Garcia-Munoz, A. Herrmann, P. Leitenstern, P. De Marne, S. Zoletnik, A. Kovacsik, J. Galdon-Quiroga, J. Rivero-Rodriguez, M. Rodriguez-Ramos, L. Sanchis-Sanchez, and J. Dominguez, Review of Scientific Instruments **89**, 10I106 (2018).
[5] P. de Marné, A. Herrmann, and P. Leitenstern, Fusion Engineering and Design **123**, 754 (2017).
[6] J. Ayllon-Guerola, J. Gonzalez-Martin, M. Garcia-Munoz, J. Rivero-Rodriguez, A. Herrmann, S. Vorbrugg, P. Leitenstern, S. Zoletnik, J. Galdon, J. Garcia Lopez, M. Rodriguez-Ramos, L. Sanchis-Sanchez, A. D. Dominguez, M. Kocan, J. P. Gunn, D. Garcia-Vallejo, and J. Dominguez, Review of Scientific Instruments **87** (2016).
[7] "CAENels FAST-PS," `https://www.caenels.com/products/fast-ps/` (2019), accessed: December-01-2020.
[8] J. P. Gunn and J. Y. Pascal, Review of Scientific Instruments **82**, 123505 (2011).
[9] A. Schmid, A. Herrmann, V. Rohde, M. Maraschek, and H. W. Müller, Review of Scientific Instruments **78** (2007).
[10] C. K. Tsui, D. A. Taussig, M. G. Watkins, R. L. Boivin, and P. C. Stangeby, Review of Scientific Instruments **83**, 10 (2012).
[11] J. Ayllon-Guerola, M. Garcia-Munoz, M. Kocan, J. Gonzalez-Martin, J. Rivero-Rodriguez, L. Bertalot, Y. Bonnet, J. P. Catalan, J. Galdon, J. Garcia Lopez, T. Giacomin, J. P. Gunn, M. Rodriguez-Ramos, R. Reichle, L. Sanchis-Sanchez, G. Vayakis, E. Veshchev, C. Vorpahl, M. Walsh, and R. Walton, Fusion Engineering and Design **123**, 807 (2017).
[12] M. Rodriguez-Ramos, M. Garcia-Munoz, M. C. Jimenez-Ramos, J. G. Lopez, J. Galdon-Quiroga, L. Sanchis-Sanchez, J. Ayllon-Guerola, M. Faitsch, J. Gonzalez-Martin, A. Hermann, P. D. Marne, J. F. Rivero-Rodriguez, B. Sieglin, and A. Snicker, Plasma Physics and Controlled Fusion **59**, 105009 (2017).
[13] T. Lunt, H. Frerichs, M. Bernert, D. Brida, D. Carralero, M. Cavedon, P. David, A. Drenik, M. Faitsch, Y. Feng, M. Griener, A. Herrmann, B. Kurzan, O. Pan, U. Plank, D. Silvagni, M. Willensdorfer, M. Wischmeier, and E. Wolfrum, Plasma Physics and Controlled Fusion **62**, 15 (2020).
[14] P. C. Stangeby, Nuclear Fusion **50**, 035013 (2010).
[15] "Ansys mechanical: Finite element analysis software," `https://www.ansys.com/products/structures/ansys-mechanical`, accessed: February-15-2021.
[16] G. Náfrádi, Á. Kovácsik, G. Pór, M. Lampert, Y. U. Nam, and S. Zoletnik, Nuclear Instruments and Methods in Physics Research, Section A: Accelerators, Spectrometers, Detectors and Associated Equipment **770**, 21 (2015).
[17] D. Dunai, S. Zoletnik, J. Sárközi, and A. R. Field, Review of Scientific Instruments **81**, 103503 (2010).
[18] H. H. Duong, W. W. Heidbrink, E. J. Strait, T. W. Petrie, R. Lee, R. A. Moyer, and J. G. Watkins, Nuclear Fusion **33**, 749 (1993).
[19] E. Hirvijoki, O. Asunta, T. Koskela, T. Kurki-Suonio, J. Miettunen, S. Sipila, A. Snicker, and S. Äkäslompolo, Computer Physics Communications **185**, 1310 (2014).
[20] M. Garcia-Munoz, S. Äkäslompolo, P. De Marne, M. G. Dunne, R. Dux, T. E. Evans, N. M. Ferraro, S. Fietz, C. Fuchs, B. Geiger, A. Herrmann, M. Hoelzl, B. Kurzan, N. Lazanyi, R. M. McDermott, M. Nocente, D. C. Pace, M. Rodriguez-Ramos, K. Shinohara, E. Strumberger, W. Suttrop, M. A. Van Zeeland, E. Viezzer, M. Willensdorfer, and E. Wolfrum, Plasma Physics and Controlled Fusion (2013).
[21] J. Galdon-Quiroga, M. Garcia-Munoz, K. G. McClements, M. Nocente, S. S. Denk, S. Freethy, A. S. Jacobsen, F. Orain, J. F. Rivero-Rodriguez, M. Salewski, L. Sanchis-Sanchez, W. Suttrop, E. Viezzer, and M. Willensdorfer, Nuclear Fusion **59**, 066016 (2019).
[22] X. Chen, W. W. Heidbrink, G. J. Kramer, M. A. Van Zeeland, M. E. Austin, R. K. Fisher, R. Nazikian, D. C. Pace, and C. C. Petty, Nuclear Fusion **53**, 123019 (2013).
[23] X. Chen, W. W. Heidbrink, M. A. Van Zeeland, G. J. Kramer, D. C. Pace, C. C. Petty, M. E. Austin, R. K. Fisher, J. M. Hanson, R. Nazikian, and L. Zeng, Review of Scientific Instruments **85**, 11E701 (2014).